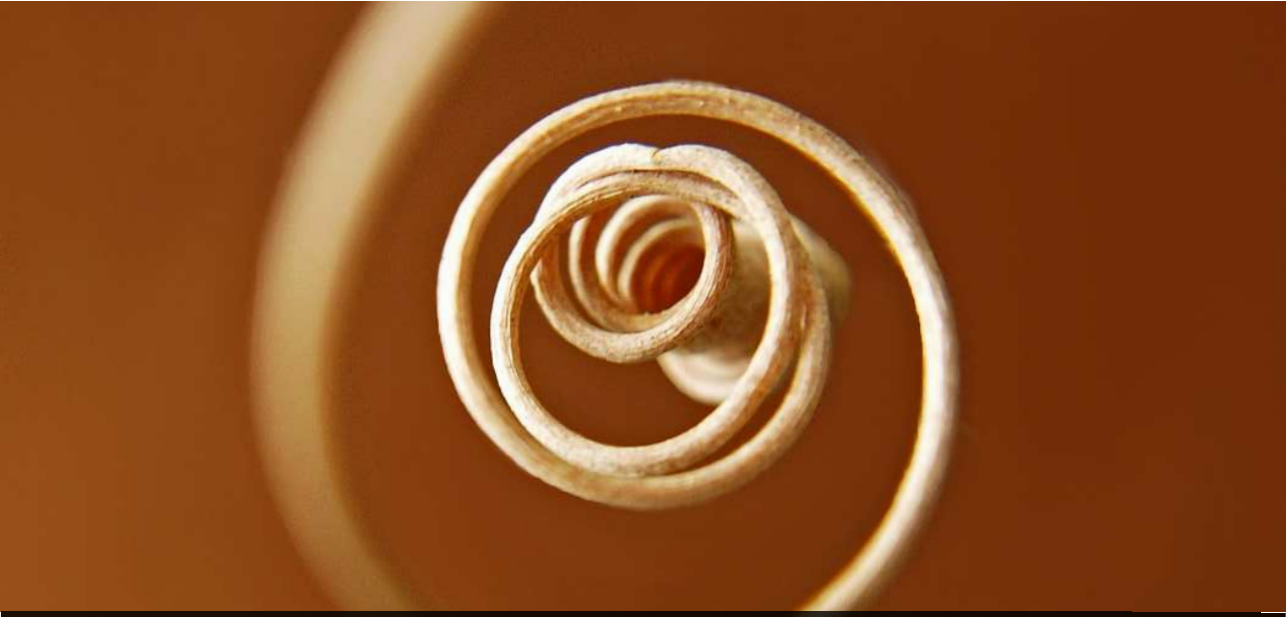


Chapter 6

Chiral Beams generated by Spiral Gratings

Abstract

Previously, zeroth order Bessel-like beams have been generated by axisymmetric diffraction gratings. Here, we report the generation of high order Bessel beams by the diffraction of plane waves over spiral shaped scatters. The acoustical beam vortex structure is analyzed and a method for generate arbitrary order Bessel beams based in multiple arms spirals is presented. A passive device is experimentally tested in the ultrasound regime and a first order Bessel vortex beam is observed. Simulations in the weak nonlinear regime are also included where the conservation law for the ratio between the topological charge of the beam and the generated harmonic order is proved. This novel technique can be used to generate cheap lenses for acoustic particle manipulation and acoustic radiation force applications.

6.1 Introduction

In the previous Chapters (4, 5) the diffraction generated by axisymmetric structures is analyzed for generate Bessel beams and strongly focused beams. Many of these axisymmetric structures, matching its symmetry with the usual sources, have been proposed for the control of the acoustic field. thus, zeroth-order Bessel-like beams can be generated by these structures in Bragg regime (Jimenez et al., 2014). In the long-wavelength limit, GRaded INdex (GRIN) lenses amplify the field in the axis (Romero-García et al., 2013; Molerón et al., 2014). In all of these configurations the scattered field maintain the axisymmetry of the lenses.

Zeroth-order Bessel beams, as those reported in Chapter 4, present a maximum of the field trough the axis. On the other hand, higher-order Bessel beams exhibit a minimum of the field at the axis. Both, zeroth and higher Bessel beams propagates in free space without any diffraction spreading, as long they are propagation-invariant solutions of the Helmholtz equation (Durnin et al., 1987). Both types of beams are characterized by the appearance of high amplitude concentric rings surrounding the axis that its transverse profile follows a lth-order Bessel function. Is important to note also that the magnitude of the spatial spectrum of these beams does not depends of the order of the beam, i.e. in the far field all Bessel beam is characterized by a annular radiation. In other words, all Bessel beams can be generated by a conical wavefront of infinite extension. The difference between zeroth and higher order Bessel beams is that for higher order Bessel beams the azimuthal phase shows a linear variation across its annular spectrum. Thus, the central zero in the axis of the higher-order Bessel beams that appears in the near field is caused due to the phase singularity of charge l associated with the azimuthal phase variations.

In this way, high order Bessel beams generates acoustical vortices with a spatial phase dependence that cannot be generated by axisymmetric radiating sources. In optics, different solutions have been proposed to break the axial symmetry in an appropriate way to generate vortices. These methods include direct Gaussian beam illumination by use of axicon-type computer generated holograms (Vasara et al., 1989; Heckenberg et al., 1992) or illuminating an axicon with a Laguerre–Gaussian mode (Arlt et al., 2000). Another solution is to impose an azimuth-dependent retardation on the optical field with Spiral Phase Plates (SPP) (Oemrawsingh et al., 2004). A diffraction grating with groove bifurcation (called "fork") is also able to generate a vortex from an optical beam falling onto the grating center with an arbitrary topological charge (Bekshaev et al., 2008).

Although phase dislocations were first studied in acoustics (Nye et al., 1974), the related experimental works have been developed lately. The acoustic analog of optical Spiral Phase Plates was proposed by Hefner et al. (1999). Here, the transducer surface is physically offset by twisting like the coil of a spring. This design has an important limitation: the transducer has a unique operating frequency of

interest. Other approaches include the use of photoacoustic effeect to generate the Helical beam (Gspan et al., 2004). A common approach to overcome this problem is by using electronic means: an appropriate phase profile for an array of transducers generates the helical beam. Thus, signals emitted by each transducer of the array are delayed in order to control the angular phase shift. The interaction of high order Bessel beams with particles have been widely studied in the exhaustive collection of works of F. G. Mitri and G. T. Silva among others. Two main remarkable effects have been reported: (1) the transference of orbital momentum from the acoustical vortex to the particle (Mitri et al., 2012), and on the other hand, the appearance of negative axial acoustic radiation forces (Marston, 2006; Marston, 2007a; Mitri, 2008; Mitri, 2009). Thus, practical applications of vortex acoustic beams are multiple: particle manipulation (Demore et al., 2011) and acoustical tweezers (Wu, 1991), an acoustic spanner (Skeldon et al., 2008), rotation of fibers (Schwarz, 2013) or multiple-particle trapping (Yoon et al., 2014). However, although the array provides active steering and control of the vortex beam, in these active methods the discretization of the source is restricted by the number of transducers in the array. On the other hand, the screw dislocations generated by finite amplitude acoustical vortex has been also studied. In the case of weak nonlinear regime, it has been proved the conservation law for the ratio between the topological charge of the beam and the generated harmonic order (Thomas et al., 2003; Marchiano et al., 2008). ON the other hand, for intense acoustic beams, azimuthal shock wave have been reported numerically and experimentally (Marchiano et al., 2008; Brunet et al., 2009; Brunet et al., 2010).

In this Chapter we propose a passive system for the formation of acoustic vortex. The design consist of an Archimedes' spiral grating. An experimental setup is proposed in the ultrasound regime, where the results show that the diffracted field around the axis generates a first order Bessel beam with its characteristic screw dislocation. A method for synthesize high order Bessel beams is also provided and tested numerically, where it was proven that a n-arm spiral generates a nth-order Bessel beam. Furthermore, weakly nonlinear propagation is considered, where the conservation law for the ratio between the topological charge of the beam and the generated harmonic order is also observed.

6.2 From axisymmetric to chiral beams

Let us start considering a pair of uniform axisymmetric gratings, A and B, as those studied before in Chapter 4. Let the grating A only differ in one aspect from the grating B: a shift in the radial position of the toroidal rings. Figure 6.1 shows a scheme of the situation. Therefore, the first structure presents a radial distribution for the M toroidal rings as $r_m = ma$, where a is the separation distance between rings and $m = (1, 2, ..., M)$ is the ring index. On the other hand, the second structure is designed as $r_m = ma + a/2$. The incident plane wave is scattered by

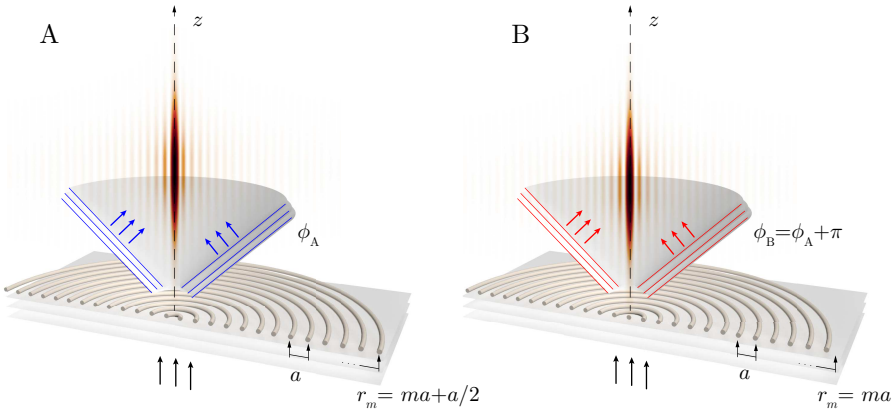


Figure 6.1: Scheme of the axisymmetric diffraction grating. The structure A differs from B by a shift of $\Delta r = a/2$ in the radial distribution of the rings. The incident plane wave is scattered by the structures in a converging conical wavefront. When it converges to the axis a Bessel beam is formed. The beams generated have equal magnitude but are shifted $\Delta\phi = 2\pi\Delta r/a$, that in this example, for $\Delta r = a/2$ leads to a phase difference of $\Delta\phi = pi$.

the structure creating a conical wavefront that converges to the axis of symmetry creating a limited-aperture Bessel beam. Same situation is also produced in the configuration B, with the only main difference of the scattered field is phase shifted.

Numerical solutions for the scattering of the two structures are shown in Fig. 6.2. It is clearly visible how the magnitude of the field remains basically the same, where the transversal field is described by a Bessel function of zeroth order, namely J_0. In the other hand, the phase difference between the structure

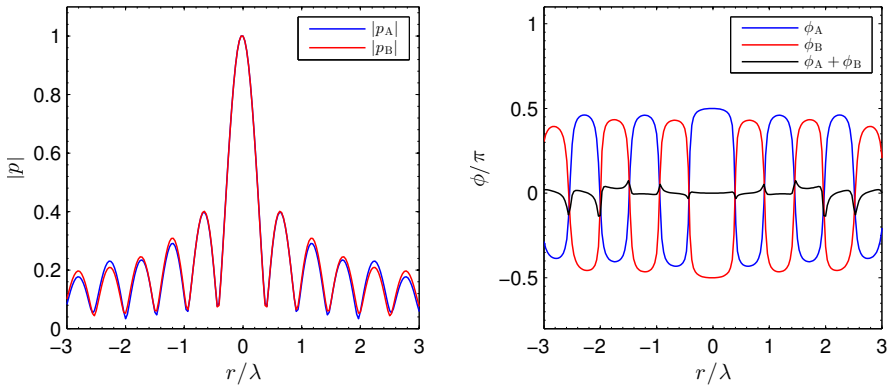


Figure 6.2: Radial distribution of the field generated by the axisymmetric structures A and B. (left) Magnitude, (right) phase. Note if the $\phi_A + \phi_B = 0$, then $\Delta\phi = \pi$.

A and the shifted grating B is π radians. The field remains in anti-phase not only at the center, but over all the the lateral lobes of the Bessel function. Only at the zeros of the Bessel function there exist in the simulations some not perfect anti-phase field distribution. In this example, the structure A is shifted in the radial coordinate by half of the radial period, this spatial shift between both structures is $\Delta r = a/2$. In a more general case, the phase difference can be related to the radial shift simply by

$$\Delta\phi = 2\pi\Delta r/a \tag{6.1}$$

where $\Delta\phi = \phi_{\mathrm{A}} - \phi_{\mathrm{B}}$ is the phase difference between fields generated by a gratings shifted a distance Δr.

Thus, we propose a structure composed of curved tubular scatters, but not necessary of toroidal shape, that mixes the properties of the gratings A and B in order to have a destructive interference in the axis. First, is obvious that this structure is no longer axisymmetric, as long the scatters at azimuth angle $\theta = 0$ must be shifted radially by $\Delta r = na/2$ respect to the plane $\theta = \pi$, being n an integer. On the other hand, the tubular scatters must be continuous in azimuth, and the following design condition

$$\phi(\theta) = \phi(\theta + \pi) \pm \pi \tag{6.2}$$

must hold for any θ. This condition is necessary in order to achieve a minimum at the axis. It essentially states that there exist a scattered field at some θ that have inverted phase respect to the scattered field at opposite azimuth $\theta + \pi$.

Let us here assume that the phase of the field changes linearly with the azimuth angle as $\phi = \alpha\theta$. Substituting this equation in Eq. (6.2) we get that, in order to fulfill the design conditions, that the rate of change of phase respect to the azimuth angle must be $\alpha = \pm 1$, leading to the simple relation $\phi = \pm\theta$.

Then, we can write Eq. (6.1) as

$$\frac{\Delta r}{\Delta\phi} = \frac{a}{2\pi}. \tag{6.3}$$

This relation states that the rate of change in the radial position of the tubes respect to the changes produced in the phase of the field is constant. Thus, using $\Delta\phi = \pm\Delta\theta$, we can relate the change of the radial position of the tubes respect to the azimuth coordinate as

$$\frac{\Delta r}{\Delta\theta} = \pm\frac{a}{2\pi}. \tag{6.4}$$

In the continuous limit, $\frac{\Delta r}{\Delta\theta} \to \frac{\partial r}{\partial\theta}$ and therefore Eq. (6.4) can be expressed as the parametric curve

$$r = \pm b\theta \tag{6.5}$$

with $b = a/2\pi$. Thus, if the tubular scatterers are bend following this parametric curve, the scattering of the structure in the axis must be zero. This expression is the Archimedes' spiral, a particular case of the general class of Archimedean spirals that can be described by

$$r = \pm b\theta^{1/\gamma}. \tag{6.6}$$

Here, the parameter γ controls how fast the spiral is wrapped. For $\gamma = 1$, we get the normal Archimedes' spiral, with uniform separation between turns, for $\gamma > 1$ the spiral radius grows with each turn, while for $\gamma < 1$ the separation distance between turns becomes thigh. Special cases of this family are the lituus ($\gamma = -2$), the hyperbolic spiral ($\gamma = -1$) or the Fermat's spiral ($\gamma = 2$).

6.3 Chiral beams generated by spiral gratings

In the previous section we have found that the spirals gratings are good candidates to provide chiral beams. These spirals have the propriety of having uniform separation between turns as $r(\theta + 2\pi) = r(\theta) + a$. This uniformly spaced grating, as occurs in the previously studied Bessel beams, diffracts plane waves in a converging conical wavefront[1]. In analogy to the well-known diffraction grating, the angle β defined by the conical wavefront is

$$\sin\beta = N\lambda/a, \tag{6.7}$$

where λ is the wavelength and N is the diffraction order. A scheme of this situation is shown in Fig. 6.3. It is well known that a converging conical wavefront generates a Bessel beam. The field of an ideal Bessel beam can be expressed for the velocity potential[2], ψ, as

$$\psi\left(r, \theta, z\right) = \psi_0 J_n\left(k_r r\right) \exp\left(i k_z z \pm i n\theta\right), \tag{6.8}$$

where J_n is the nth-order Bessel function ψ_0 is the amplitude, and k_z and k_r are axial and transverse components of the wavevector $k = \sqrt{k_z^2 + k_r^2}$. It is important the relation of this quantities to the cone angle of the Bessel beam

$$\cos\beta = k_z/k \ , \ \sin\beta = k_r/k. \tag{6.9}$$

[1]Note that the field is also scattered in a diverging cone with angle $\pi/2 - \beta$, but this waves does not contributes to the field distribution near the axis in free propagation. If the structure is embedded inside a tube, this field can be reflected by the boundaries and it will converge to the axis creating another Bessel beam.

[2]the velocity potential can be related to the acoustic pressure as $p = i\omega\rho_0\psi$ and to particle velocity as $\mathbf{v} = \nabla\psi$

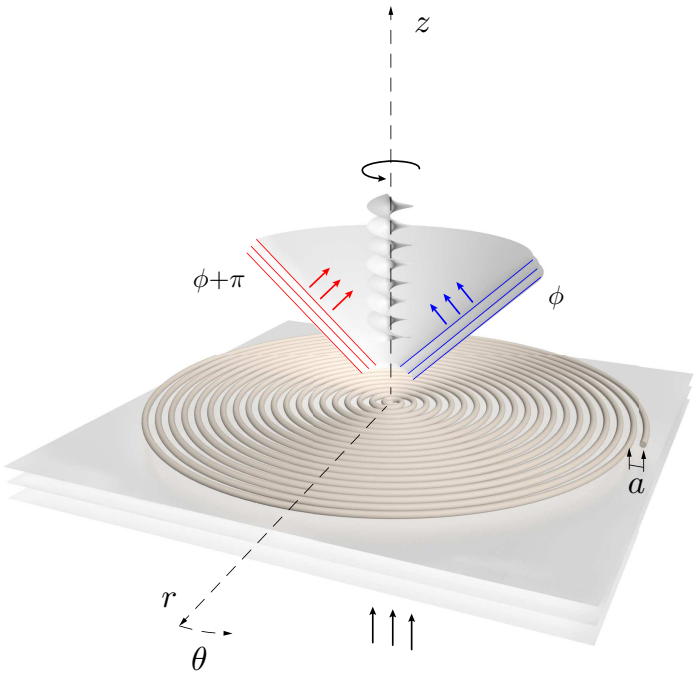


Figure 6.3: Scheme of the Archimedes' spiral scattering process. The incident plane wave is scattered into a converging conical wavefront which its phase changes linearly in azimuthal angle θ. The field can be described as a first order Bessel beam, where in the axis a corkscrew dislocation is produced, leading to an acoustic vortex and a node at $r = 0$.

Note the trivial solution for $\beta = 0$, where the Bessel beam reduces to a plane wave traveling in the z direction. Therefor, thee cone angle β of the Bessel beam depends on the separation of scatters. Thus, combining Eq. (6.7) and (6.9) we get the relations

$$k_z = \frac{2\pi N}{a \tan \beta} \ , \ k_r = \frac{2\pi N}{a}. \tag{6.10}$$

This relations allow us to obtain the Bessel beam field, Eq. (6.8) in terms of the grating parameters as

$$\psi\left(r, \theta, z\right) = \psi_0 J_n \left(\frac{2\pi N}{a} r\right) \exp\left(i \frac{2\pi N}{a \tan \beta} z \pm in\theta\right). \tag{6.11}$$

This idealized field is valid for a grating of infinite aperture. In the case of a real

structure with finite aperture, the Bessel beam is bounded in the axial direction. Is common to refer to this limitation as limited diffraction Bessel beams. Therefore, if the grating have a total aperture of $R = Ma$, where M is the number of turns of the spiral, from simple trigonometrical considerations the cone angle will cover a region of the axis from $z = 0$ to $z = F$, being

$$F = \frac{R}{\tan\beta} = \frac{Ma^2}{N\lambda}\sqrt{1 - \left(\frac{N\lambda}{a}\right)^2} \tag{6.12}$$

the maximum distance at which the Bessel beam is formed, showing the limit of the validity of the nondiffractive propagation.

Let us consider the radiation converging from each ring at angle β, in order to find the locus of the points around the axis where exact constructive interference is produced. The spiral grating is not axisymmetric, but chiral, that is, it is distinguishable from its mirror image and it cannot be superposed onto it. Thus, the radiation converging from each ring do not converge along the symmetry axis. Figure 6.4 shows a scheme, where if we suppose the grating diffracts the wave at angle β, and following simple trigonometry considerations the coordinates of the focal points can be obtained in function of the spiral geometry. Thus, for the axial component of the focal can be expressed as

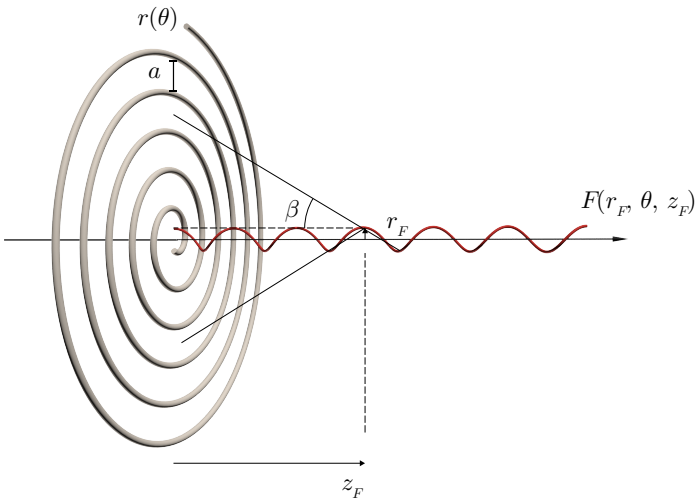


Figure 6.4: Scheme of the geometry of the spiral. Due to the scattering of the spiral at angle β, the locus of points in which perfect constructive interference is produced around the axis is an helix.

$$z_F(r,\theta) = \frac{r(\theta) + \frac{a}{4}}{\sin\beta}\sqrt{1-\sin^2\beta}. \tag{6.13}$$

Then, using the cone angle definition and the spiral curve $r(\theta)$ we get

$$z_F(\theta) = \left(\frac{\theta}{2\pi} + \frac{1}{4}\right)\frac{a^2}{N\lambda}\sqrt{1-\left(\frac{N\lambda}{a}\right)^2}. \tag{6.14}$$

On the other hand, this interference is not produced at the axis, but shifted a constant radial distance. From the geometry, see Fig 6.4, we can see that the radial component of the focal is

$$r_F = a/4. \tag{6.15}$$

Equations (6.14-6.15) composes the curve $F(r_F, \theta, z_F)$, that is a liner helix of constant radius. Thus, in addition the beam generation, the scattering located in the points of the spiral achieves perfect constructive interference over the helix curve that rotates around the axis. Moreover, the distance between turn of this helix can be calculated as $z_F(\theta + 2\pi) - z_F(\theta) = \lambda\cos\beta/N$. Thus, for small diffraction angles, the focal rotates in z with a period of the order of the wavelength, when for shorter Bessel cone is generated, the distance between rotation in the helix stretches[3].

6.3.1 First order Bessel beams

Let us now analyze the Archimedes' spiral with $\gamma = 1$ and $b = a/2\pi$. With this parameters the ideal Bessel beam can be expressed as

$$\psi(r,\theta,z) = \psi_0 J_n\left(\frac{N}{b}r\right)\exp\left(i\frac{N}{b\tan\beta}z \pm in\theta\right). \tag{6.16}$$

In the other hand, we model the scattering of the grating by two methods. First, if the scatters are thing compared to the wavelength, we can assume the scattering of each fragment of the spiral can be modeled by a point source. This modeling is also valid in the opposite limit, where the scatterers are thick enough to provide narrow aperture between them. In this situation the structure forms a grating. From Babinet's principle considerations, both situations can be equivalent. Therefore, we calculate the Rayleigh-Sommerfeld diffraction integral along the path of the spiral, $r = b\theta$, as

$$p(x,y,z) = \frac{-i\omega\rho_0 v_0}{2\pi}\int_r \frac{\exp(ik|\mathbf{r}|)}{|\mathbf{r}|}dr \tag{6.17}$$

[3]In the limit $\beta \to 0$, where the helix period is the wavelength, the divergent and convergent conical wavefront sums again into a plane wave. Thus, the helicity disappears due to the topological charge of two chiral waves is inverted.

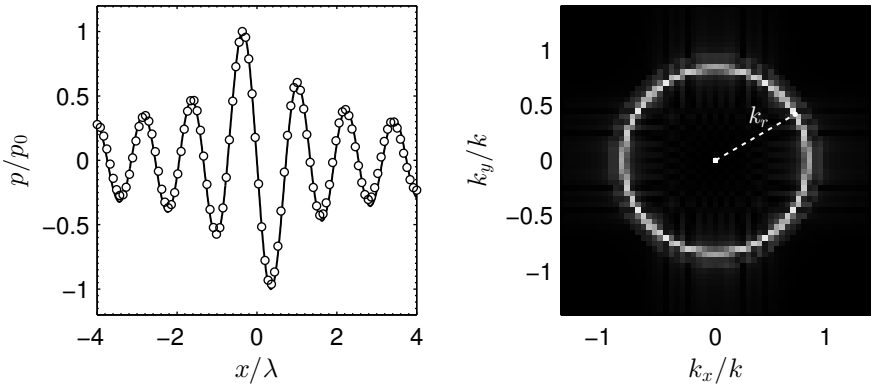


Figure 6.5: (Left) Transversal cut of beam field obtained by (continuous line) the analytic expression for ideal Bessel beam Eq. (6.16) and (circles) obtained by numerical evaluation of the Rayleigh-Sommerfeld diffraction integral Eq. (6.17) for a finite structure. (Right) Far-field of the spiral scattering showing the typical ring of the Bessel beam.

where $|\mathbf{r}|$ is the distance between each point in the path, $r = b\theta$, and the observation point (x, y, z).

Second, we also approximate the diffraction with full-wave numerical integration of the acoustic wave equations. This approach provides an accurate estimation of the diffraction in situations where the wavelength is of the order of the scatter size, but due to the problem is 3D, the full cartesian domain is integrated and is computationally intensive. In order to reduce the grid refinement requirements, we use the k-space method for solving the 3D computational problem. This method will be necessary also for the last section where we include the nonlinear propagation effects.

Figure 6.5 shows an example of first order Bessel-like beam generated by an uniform spiral with parameters $\beta = 56.4^{\text{o}}$, $a/\lambda = 1.2$ and aperture $R = 60\lambda$. We can see that the analytic expression for ideal Bessel beam Eq. (6.16) agrees with the solution obtained by the numerical evaluation of the Rayleigh-Sommerfeld diffraction integral Eq. (6.17) for this finite structure. On the right subplot, it can be appreciated how the typical ring of the Bessel beam appears in the far-field. This result shows that a conical wavefront is being generated by the structure, and it can be seen that the transversal wavenumber agrees with the estimated by the spiral parameters in Eq. (6.10), marked as a dotted line as k_r in the figure. Therefore, we prove the field generated by the spiral structure is a first order Bessel-like beam.

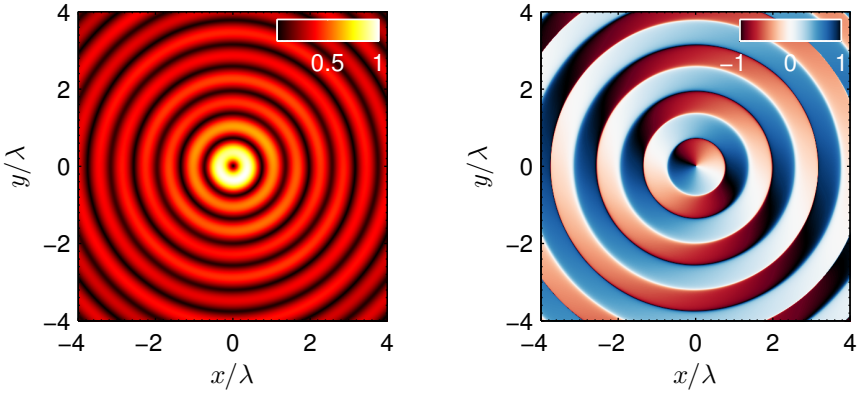


Figure 6.6: Transversal distribution of the field obtained by numerical evaluation of the Rayleigh-Sommerfeld diffraction integral. (Left) Magnitude, (right) phase. Colorbars in normalized units (p/p_0 and ϕ/π).

Radial distribution: vortex

One of the main features of the high order Bessel beams (HOBBs) is that all over the axis the field is zero, in contrast with the zeroth-order Bessel beam where a maximum appears in the symmetry axis. In the high order Bessel beams this zero is generated by destructive interference of a phase-rotating conical wavefront. Therefore, as a necessary condition, a vortex is generated around the axis. Figure 6.6 shows the transversal distribution of the field of a spiral at $F/2$. It can be observed the node at the center in the magnitude, as long the high amplitude lateral lobes characteristic of the HOBBs.

On the right subplot, it can be appreciated that a vortex is generated. The number of complete phase shifts per turn is one, the vortex presents a topological charge of 1. The nodes of the field connects 2 areas with opposite phase, while at the central minimum a screw-cork like dislocation is produced in the field. The ringed areas of the phase distribution corresponding to odd lateral lobes are phase inverted respect than the even ones, but all have the same rotation direction.

Axial distribution

Although the field distribution in the sagittal plane correctly corresponds to a truncated Bessel beam, there exist some features that must be underlined. Figure 6.7 shows the field in the ($x = 0$) plane of two first order Bessel beams. In the top subplot the spiral parameters are $a/\lambda = 1.85$, that leads to a cone angle of $\beta = 32.7^{\text{o}}$ and a beam extension distance of $F = 115\lambda$. As can be seen in the figure, the generated beam agrees with the analytical parameters. However, the farther part of the beam that is close to F presents more amplitude compared to

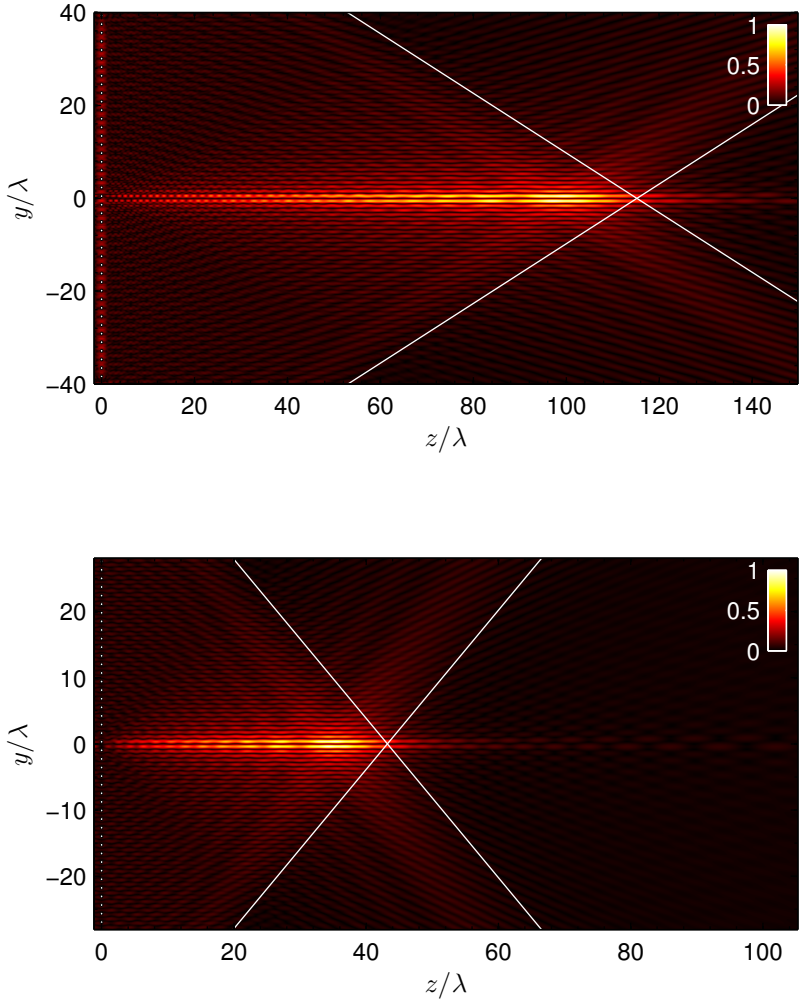


Figure 6.7: (Top) Distribution of the field for a spiral of $a/\lambda = 1.85$ that leads to a (white line) cone angle of $\beta = 32.7^{o}$ and beam extension distance of $F = 115\lambda$ (white line at $y = 0$). (Bottom) Distribution of the field for a spiral of $a/\lambda = 1.3$ that leads to a (white line) cone angle of $\beta = 50^{o}$ and beam extension distance of $F = 43.2\lambda$ (white line at $y = 0$). Colorbars in normalized units ($p/p_{\max}$).

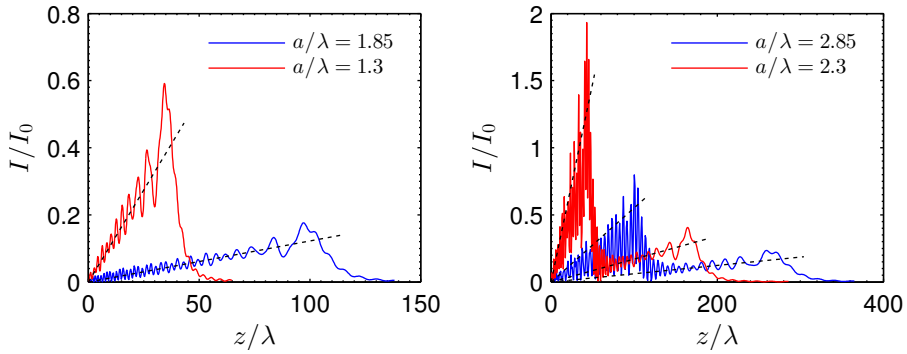


Figure 6.8: (Left) Axial Intensity distribution for a spiral of (blue) $a/\lambda = 1.85$ and (red) $a/\lambda = 1.3$. Black dashed lines shows the analytical extension of the truncated beam with a linear intensity profile. (Right) Axial Intensity distribution including higher diffraction orders for a spiral of (blue) $a/\lambda = 2.85$ and (red) $a/\lambda = 2.3$.

the part of the beam that is close to the grating. On the other hand, the field also present some oscillations in the z direction.

Figure 6.7 (bottom) shows other example at lower frequency. Here, the spiral parameters are $a/\lambda = 1.3$, that leads to a sharper cone angle of $\beta = 50^{\text{o}}$ and a closest extension distance of $F = 43.2$. Same properties can be observed in this situation.

In order to analyze the field amplitude, a axial cut is represented in Fig. 6.8. As long the field is zero in the axis, the intensity distribution shown in Fig. 6.8 is evaluated trough the maximum of the first lateral lobe. It can be clearly seen that the intensity increases linearly with the axial distance. This effect, is analogous to the studied in Sec. 4.2. As long the outermost rings scatters more energy, the external portions of the conical wavefront present more intensity. This energy converges to axial points around F, creating the same Bessel beam but with linearly increasing intensity.

Same effects are observed for the higher diffraction orders. As can be seen in Fig. 6.8 (right), when $a/\lambda > 2$ the higher diffraction orders generates a secondary beam. Its corresponding parameters correctly follows the analytical estimations, as can be seen comparing the beam distribution to the dashed black lines. Due tho the appearance of this secondary beam, the amplitude of the fundamental diffraction order is reduced.

A parametric study of the longitudinal field is presented in Fig. 6.9 (left). It is analogous to the Fig. 4.2 for the zeroth-order Bessel beams. The field distribution extends with frequency following the analytical estimations (white lines), and for $a/\lambda > 2$ higher diffraction orders appears forming secondary Beams close to the grating. On the other hand, similar study can be addressed for the transversal

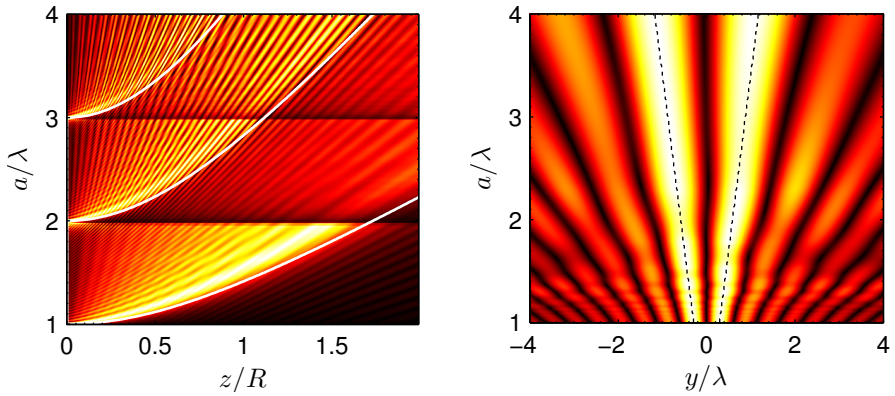


Figure 6.9: (Left) Axial distribution of the field in function of the quantity a/λ obtained by numerical evaluation of the Rayleigh-Sommerfeld diffraction integral. White lines indicates the estimation of the focal by Eq. (6.12). (Right) Transversal distribution of the field in function of the quantity a/λ. Black dotted lines indicates the lateral location of the lobes estimated by Eq. (6.16). Colorbars in normalized units (p/p_0 and ϕ/π).

distribution. Figure 6.9 (right) shows the lateral distribution normalized to the wavelength in both axes. The separation distance is varied. As long the lateral distribution of the HOBBs depends on the transversal component of the wavevector, $k_r = 2\pi N/a$, there exist a lateral dependence of the lateral beam-width respect to spiral parameters. It essentially states that extending the Bessel beam at longer distances by spacing the spiral also spreads the beam-width. The numerical integration agrees with the analytical estimations (dashed black lines).

6.3.2 Experimental validation

An experimental test was realized in order to validate model results. A spiral grating was fabricated by laser cutting over a stainless steel plate of 0.8 mm thickness. Fig. 6.10 (a) shows a scheme of the grating designed. The grating aperture was $a = 1$ mm. The thickness of the scatters was 0.75 mm (solid parts), leading to a grating aperture of 0.25 mm (open parts)[4]. The number of turns was $M = 20$ and the grating radius was $R = 25$ mm. The circular spiral plate was placed in front of a ultrasound plane transducer. This source was formed by a plane single element piezoceramic crystal (PZ 26, Ferroperm Piezoceramics, Denmark) mounted in a custom designed steel housing with aperture $R = 25$ mm, matching the area of the spiral grating. The separation distance between the grating and the source plane was adjusted to 0.5 mm.

[4]As pointed before, following Babinet's principle considerations, the scattered field by an structure of thin scatters or thin slits, in terms of the generated beam profile over the axis, is equivalent.

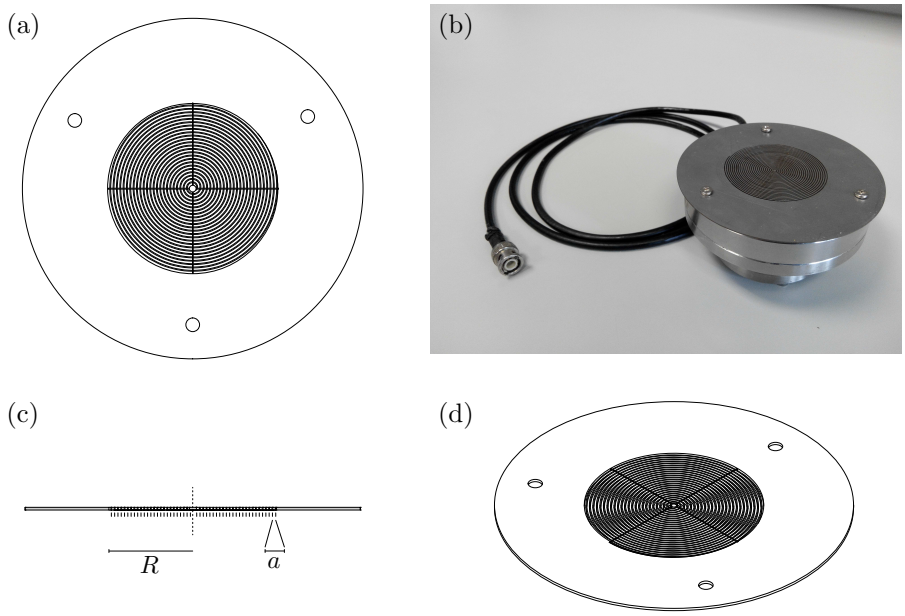


Figure 6.10: (a, c, d) Scheme of the grating used in the experiment. (b) The spiral grating mounted in front of a plane ultrasound transducer.

The transducer was immersed in a degassed and distilled water tank of ($350 \times 350 \times 350$ mm) were during the measurements the temperature was constant at 26° C. Therefore, the theoretical beam extension distance of the proposed grating lens at the operating frequency was $F = 27$ mm and only one diffraction order appear.

The source was driven with a sinusoidal pulse burst of frequency $f_0 = 2.226$ MHz and 50 cycles using a function generator (14 bits, 100 MS/s, model PXI5412, National Instruments) and a linear RF amplifier (ENI 1040L, 400W, 55dB, ENI, Rochester, NY). The pressure waveforms were acquired with a HNR 500 μm needle PVDF hydrophone (Onda Corp, CA), and a digitizer (64 MS/s, model PXI5620, National Instruments) were used. A three-axis micropositioning system (OWIS GmbH, Germany) was used to move the hydrophone in three orthogonal directions with an accuracy of 10 μm and a National Instruments PXI-Technology controller NI8176 was used to control all the devices. The amplitude frequency response of the hydrophone was compensated in post-processing.

Figure 6.11 summarizes the experimental and numerical results, and the Rayleigh-Sommerfeld integration. It can be observed in Fig. 6.11 (a) that the steel grating conform a beam with a zero in its axis, and with a ring shaped maximum surrounding this zero. The experimental beam agrees the analytical Bessel beam presented in Fig. 6.11 (c). On the left column, the phase is shown and, again,

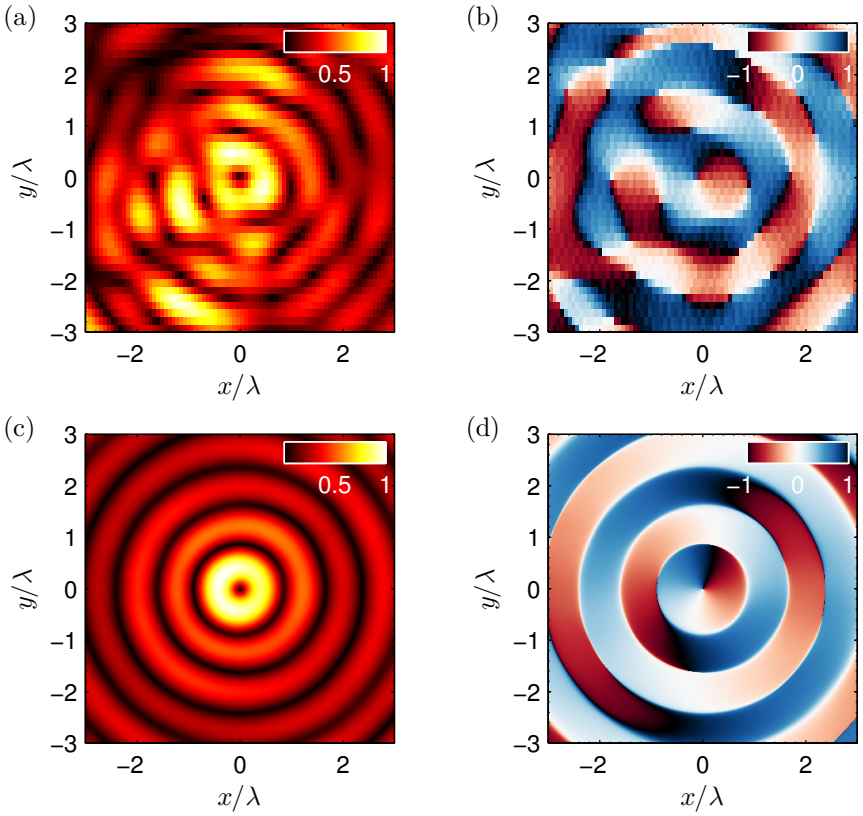


Figure 6.11: (a) Normalized field magnitude and (b) phase observed in the experiment and (c, d) its corresponding analytical estimation using Rayleigh-Sommerfeld integration. Colorbars in $p/p_{\max}$ units for the magnitude and ϕ/π units for the phase.

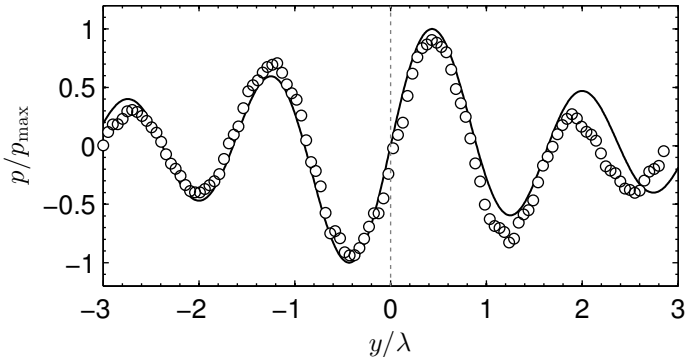


Figure 6.12: Transversal cut of the field observed by (circles) grating experiment and (line) predicted by the HOBB. Vertical line marks the axis were the zero field is expected.

the generated beam in the experiment shows the correct topological charge of the analytic solution plotted in Fig. 6.11 (d). The characteristic screw-cork dislocation of the field at the center is also observed. Moreover, the phase distribution all over the secondary lateral lobes of the beam also shows, in some degree, the correct phase distribution of the HOBB.

However, some discrepancies can be observed in the experimental measurements. These aberrations are minor and can be produced by the misalignment between the grating and the transducer plane. A detailed transversal field profile is presented in Fig. 6.12. The transversal cut (markers) was selected for an azimuthal angle in the (y, x) plane at -3 degrees, in order to present a good fit with the analytical solution (black line). The traversal profile correctly agrees its corresponding $J_1(k_r r)$ first order Bessel function. Minor aberration slightly modifies the lateral lobe amplitude, but the main features of the high order Bessel beam, i.e. its central zero and rotational vortex, are correctly observed by the proposed (and simple) experimental setup.

6.4 High order Bessel beams generated by n-arm spirals

In the preceding section a synthesis of first order Bessel beams is proposed. The basic principle of formation is the destructive interference trough the axis of a rotating-phase conical-wavefront. The phase rotation over a turn in the cone was 2π, and the topological charge of the generated vortex was 1. Here, we extend this idea in order to generate vortex with higher topological charge. Therefore, the phase rotation of the cone must increase for each turn as $n2\pi$. Applying same ideas developed previously, Eq. (6.1), we must increase the spiral radius r as $r(\theta) = nb\theta$ in order to increase the rotation of the phase by $n2\pi$.

However, if the spiral is constructed in that way, the spacing between turns is increased from a to na, and therefore, higher diffraction grating will appear and energy will spread into a multi focal beam as shown in Fig.6.8. Actually, the higher diffraction grating orders of a spiral generates high order Bessel beam. The beams presented in Fig.6.8 (right) corresponding to the diffraction order $N = 2$ were second order Bessel beams. Figure 6.13 shows a more clear example. There, in the left subplot a first order Bessel beam is generated at $a/\lambda = 1.2$. On the right, the frequency is increased to match $a/\lambda = 7.2$, the beam of the first order is generated far a way from the grating plane. Near the source appear the higher diffraction gratings. The profile of the 7th diffraction grating order generates a 7th order Bessel beam, where it can be appreciated that the numerical integration correctly agree the analytical estimation using $N = 7$. Therefore, HOBBs can be generated from the higher diffraction grating of a simple Archimedes' spiral.

For practical applications it must be desirable to generate a single HOBB

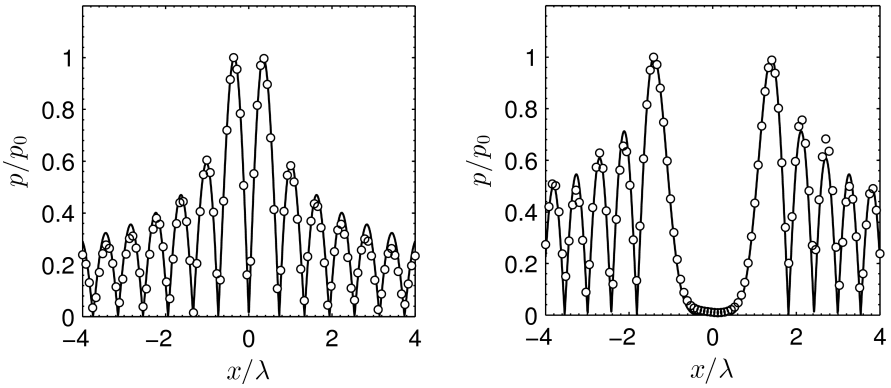


Figure 6.13: Generation of a high order Bessel beam from higher diffraction orders of a simple Archimedes' spiral grating. (continuous line) Analytical solution with (left) $N = 1$ and (right) $N = 7$, (circles) numerical integration at a distance $z = F(N)/2$

without any diffraction orders in order to do not spread energy from the main beam to other secondary spots, e.g. in addition to the previously 7th order Bessel beam of Fig. 6.13, all the inferior order Bessel beams are generated together.

The only way to increase the radius of the spiral as $r(\theta) = nb\theta$, while maintaining the grating spacing between turns, a, is to add additional arms to the spiral that fills the space between the stretched new curve. The general expression of n-arms spiral is

$$r_j = nb\left(\theta + j\frac{2\pi}{n}\right). \tag{6.18}$$

Therefore, there exists n curves, each j curve is separated a distance a from its adjacent curve, and each curve start from the origin at different angles, equispaced $2\pi/n$. Figure 6.14 shows various spirals with increasing number of branches. In the case of $n = 2$, it can be observed that the curve for the $j = 1$ branch (black spiral) have a growth slope of $\Delta r/\Delta\theta = 2b$. Therefore, the phase rotates at $\Delta\phi = \Delta\theta = 2$. Same applies to the second arm, but this arms maintain the separation between turns constant, allowing the generation of the Bessel conical wavefront for the first diffraction order. As Fig. 6.14 shows, other possibilities are also feasible in order to obtain higher spiral arms. The main issue is that when the number of arms increases the aperture between them does not remain constant near the center, when obviously in the limit $n \to \infty$, the structure becomes completely opaque if it is formed by finite sized scatterers, or in-existent if the grating is formed by finite sized slits.

As long the spacing between spiral arms is kept constant at a distant a, the diffraction produced by the grating will create a cone with same angle that for

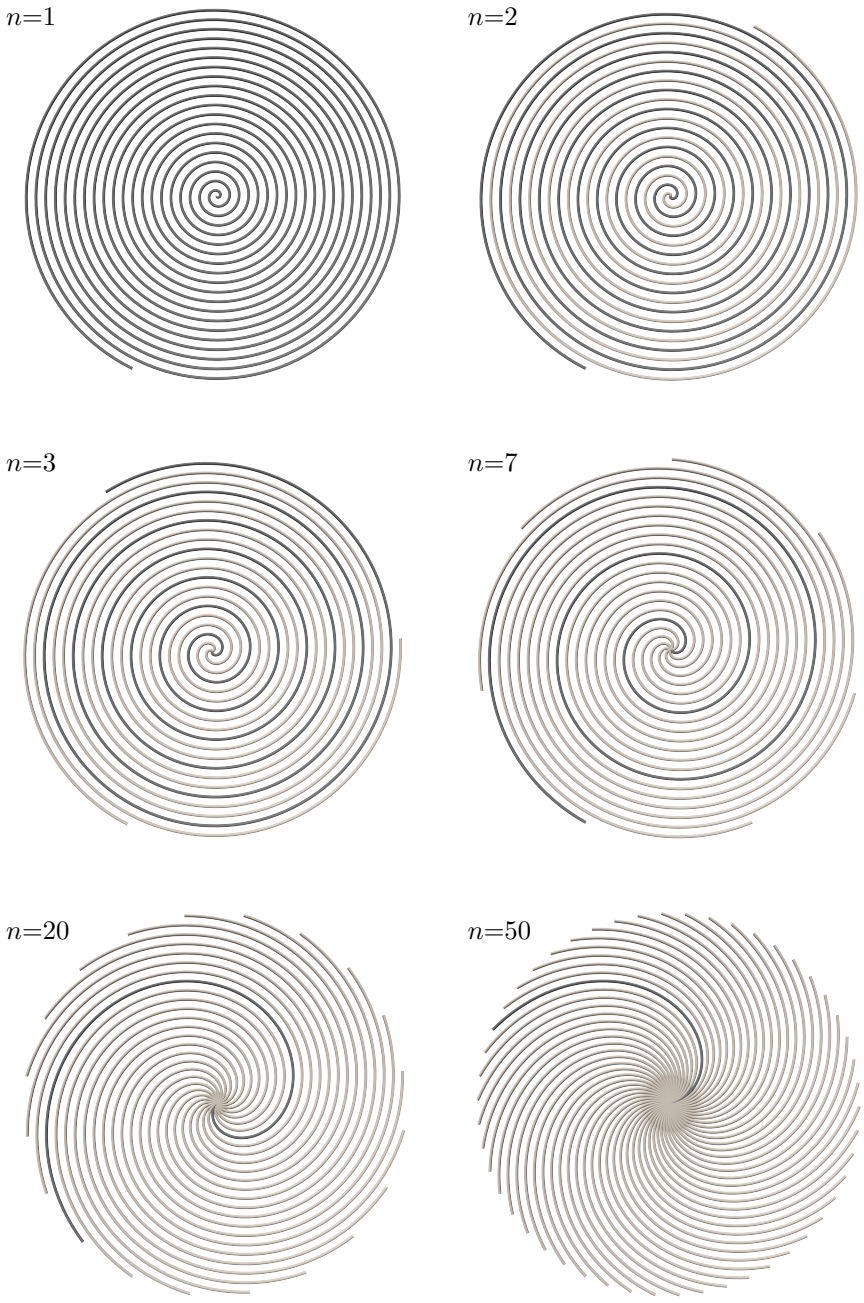


Figure 6.14: Scheme of a variety of n-arm spirals.

the first order Bessel Beams. When this conical wavefront converges to the axis, a Bessel beam is also generated. However, due to the rotation of the phase is increased by a factor of n, the corresponding beam is a nth-order Bessel beam. It can be appreciated in the last term of Eq. (6.11), that the topological charge will also be increased by a factor n. The number of arms of a spiral directly corresponds to the order of the Bessel beam generated and therefore to the topological charge of the acoustical vortex.

Beam profiles of the generated HOBBs are presented in Figs. 6.15-6.17. The magnitude of the field transversal sections are shown in Fig. 6.15 for n-arm spiral gratings of $n = 1, 2, 3, 7, 20, 50$. Here, the grating parameters were selected as $a/\lambda = 1.2$ and $\beta = 56.4^{\circ}$. First, in Fig. 6.15 we represent a transversal cut of the field measured at $z = F/2$. As can be seen, the field is zero at the axis of the beam, and the central null spot increases in size according to the number of branches of the spiral. The generated field is nearly zero in a cylindrical volume around the axis: the higher the number of arms of the spiral, the bigger the volume around the axis where the field is nearly zero. Even in the case of a 50 branches spiral, the generated beam profile agrees with a 50th order Bessel beam. In this case, the corresponding central null is generated over a roughly cylindrical volume of 18 λ diameter (in agreement to Eq. (6.16) and a height of F (in agreement to Eq. (6.12).

The location of the ring shaped lateral lobes, where the field increases to its maximum, also matches the beam profile of the function $J_n(2\pi/ar)$. A close comparison will be presented later. On the other hand, it can be appreciated that the ringed lateral lobes present some oscillations or bumps. They are more evident in the higher order Bessel beams. If the transverse plane where the measurement is done moves from $z = F/2$ to $z = F/2 + \Delta F$, these oscillation rotate around the axis. Furthermore, the number of oscillations is proportional to the order of the Bessel beam. They can be associated to the geometrical laws of perfect constructive interference around the axis for each arm of the spiral, in analogy to Eq. (6.14). Therefore, this results shows evidence of that the focal $F(r_F, \theta, z_F)$ for n-arms develop equispaced n helix curves that rotates around the axis.

On the other hand, the phase of the nth-order Bessel beam rotates around the axis forming an acoustic vortex. As can be seen in Fig. 6.16, the topological charge of the beam, i.e. the number of $n2\pi$ phase increments in a turn, is proportional to the number of branches. Furthermore, it is in agreement with the n-th order phase rotation characteristic HOBBs. These features are specially visible around the ringed areas of the field in which the field is maximum, according to Fig. 6.15.

Figure 6.17 shows the magnitude over the $(x = 0)$ plane. The generated beams correctly agrees with the truncated HOBBs. The extension of the minimum at the axis is in all cases $F = XXX\lambda$. Another feature is that in the case of higher n, i.e. $n = 50$, the extension of the maximum lateral lobe ring is shorter. This is due to the finite size structure, the beam only can be formed in the volume sonificated

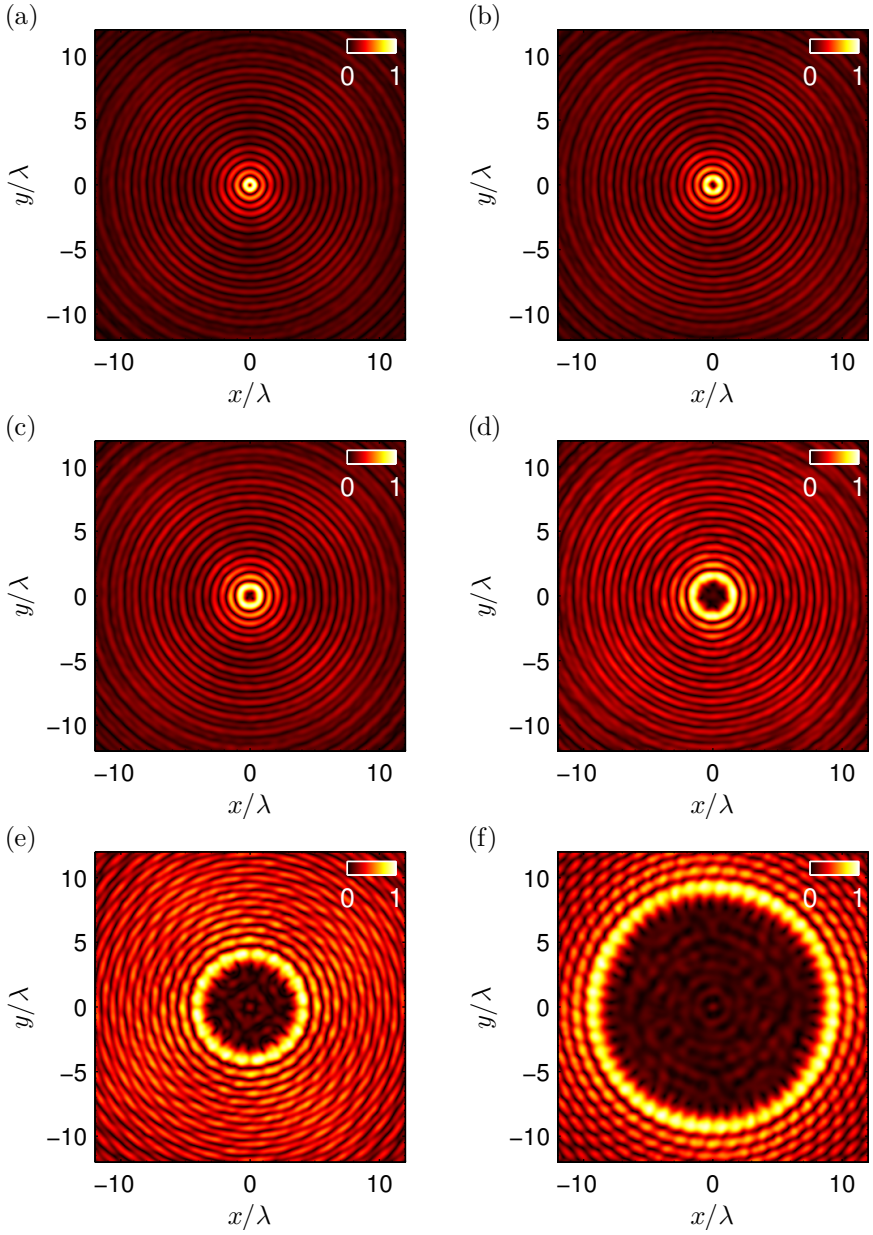


Figure 6.15: Magnitude of the transversal section of the field generated by a n-arm spiral grating, from (a-f), $n = 1, 2, 3, 7, 20, 50$. Colorbars in $p/p_{\max}$ units.

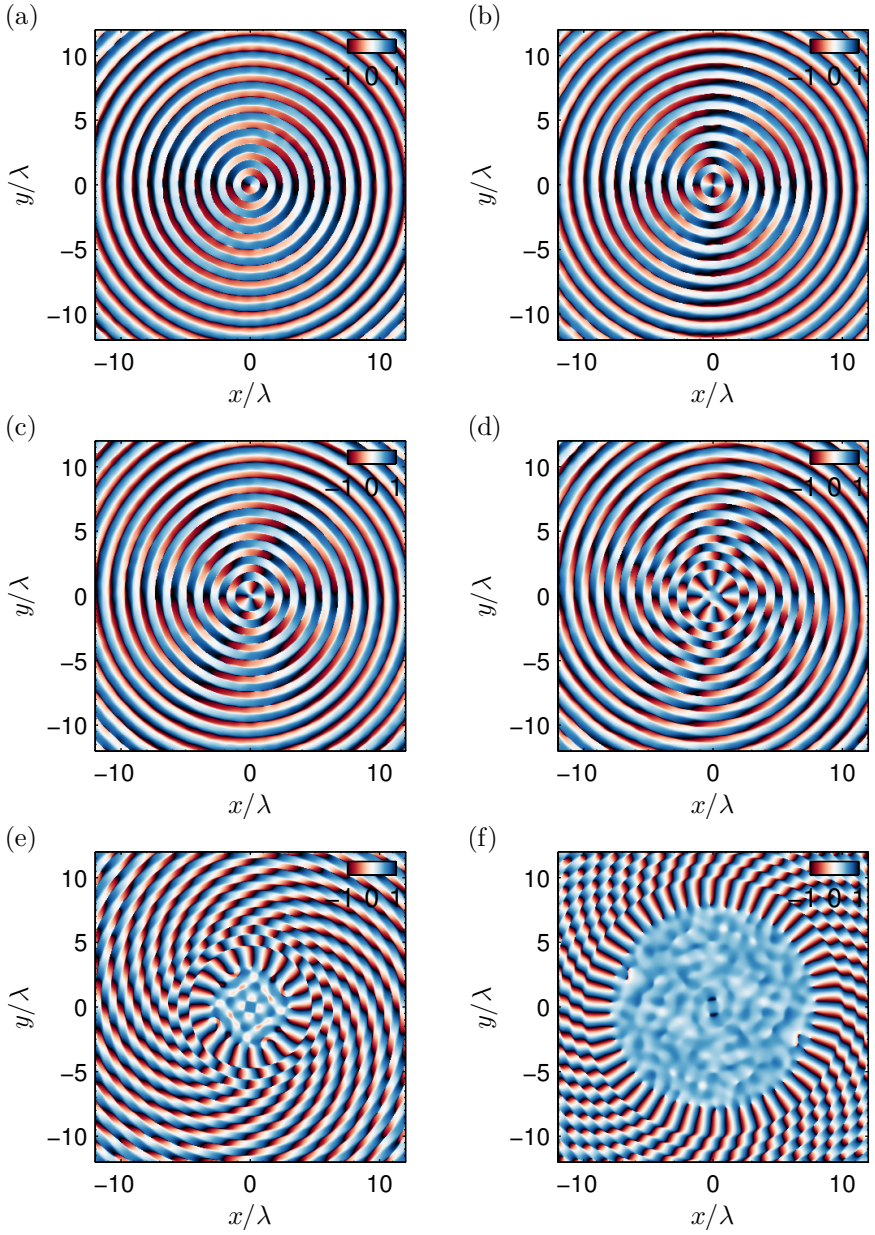


Figure 6.16: Phase of the transversal section of the field generated by a n-arm spiral grating, from (a-f), $n = 1, 2, 3, 7, 20, 50$. Colorbars in ϕ/π units.

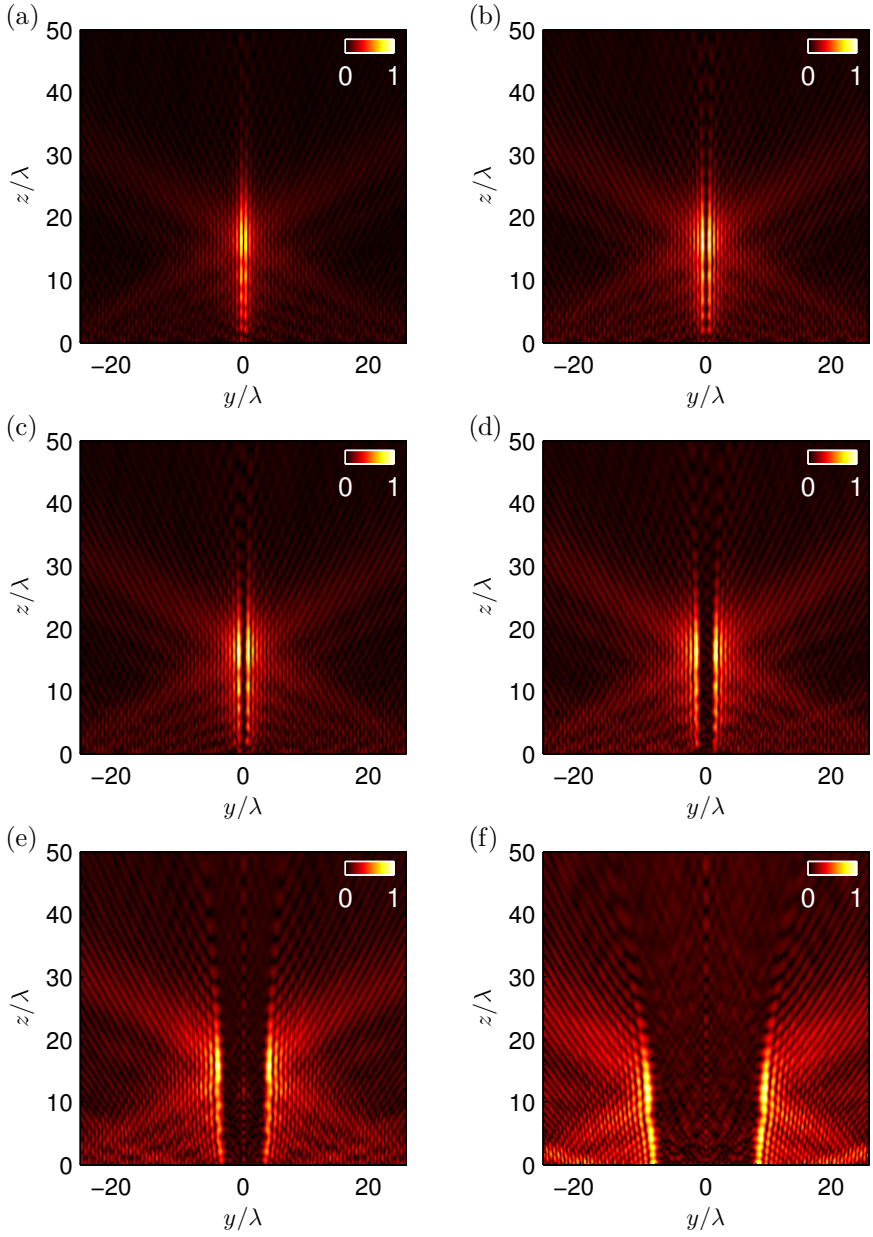


Figure 6.17: Magnitude of the axial distribution of the field for the n-arm spiral grating, from (a-f), $n = 1, 2, 3, 7, 20, 50$. Colorbars in $p/p_{\max}$ units.

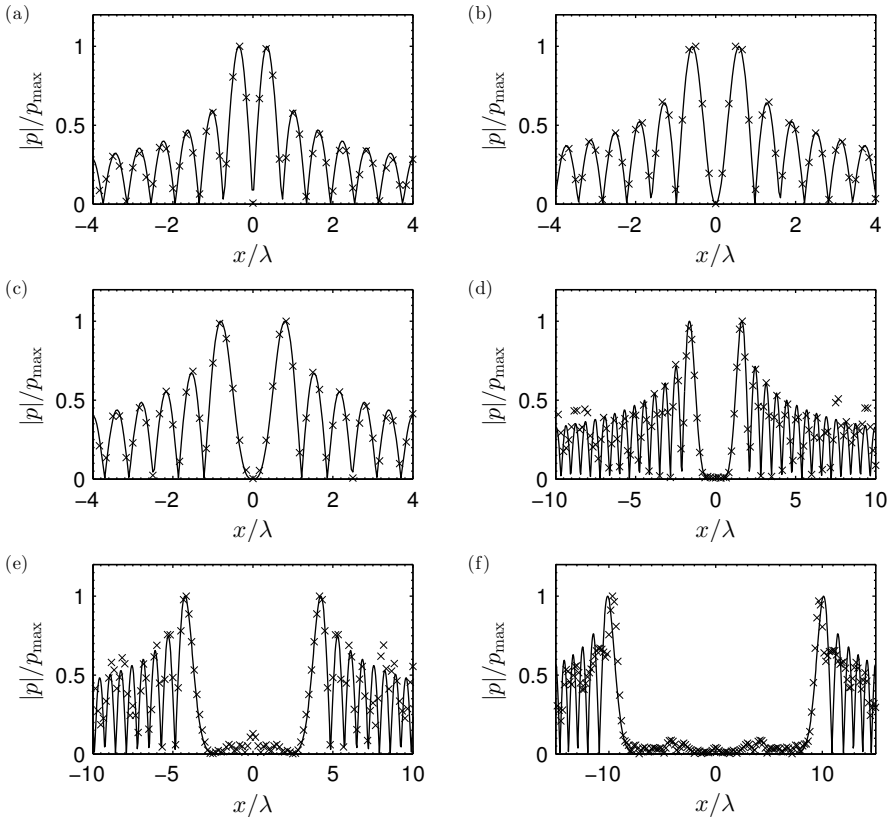


Figure 6.18: Magnitude of a transversal cut of the field for the n-arm spiral grating, from (a-f), $n = 1, 2, 3, 7, 20, 50$. (Markers) k-space numerical simulation, (continuous line) analytical HOBBs solutions.

by the conical wavefront. This volume extends from $z = 0$ to $z = F$ at the axis, but for radially distant points, this distance is reduced. Any case, this limitation does not impedes the correct formation of the truncated Bessel beam, even in the case of $n = 50$.

In order to demonstrate the multiple helix that conforms the acoustic vortex, we can represent the isosurface of the equal phase points. The modulations in the field magnitude over the rings of the high order Bessel beam correctly matches the helical shape shown of this reconstructed Fig. 6.21, in analogy with the analytical locus by Eqs. (6.14-6.15). The number of helix arms is equal to the number of spiral arms of the gratings, and its radius grows also withe the order of the Bessel beam generated.

Finally, in order to study these beams in a more realistic configuration, simulations of the full 3D problem of the same system were performed. In these

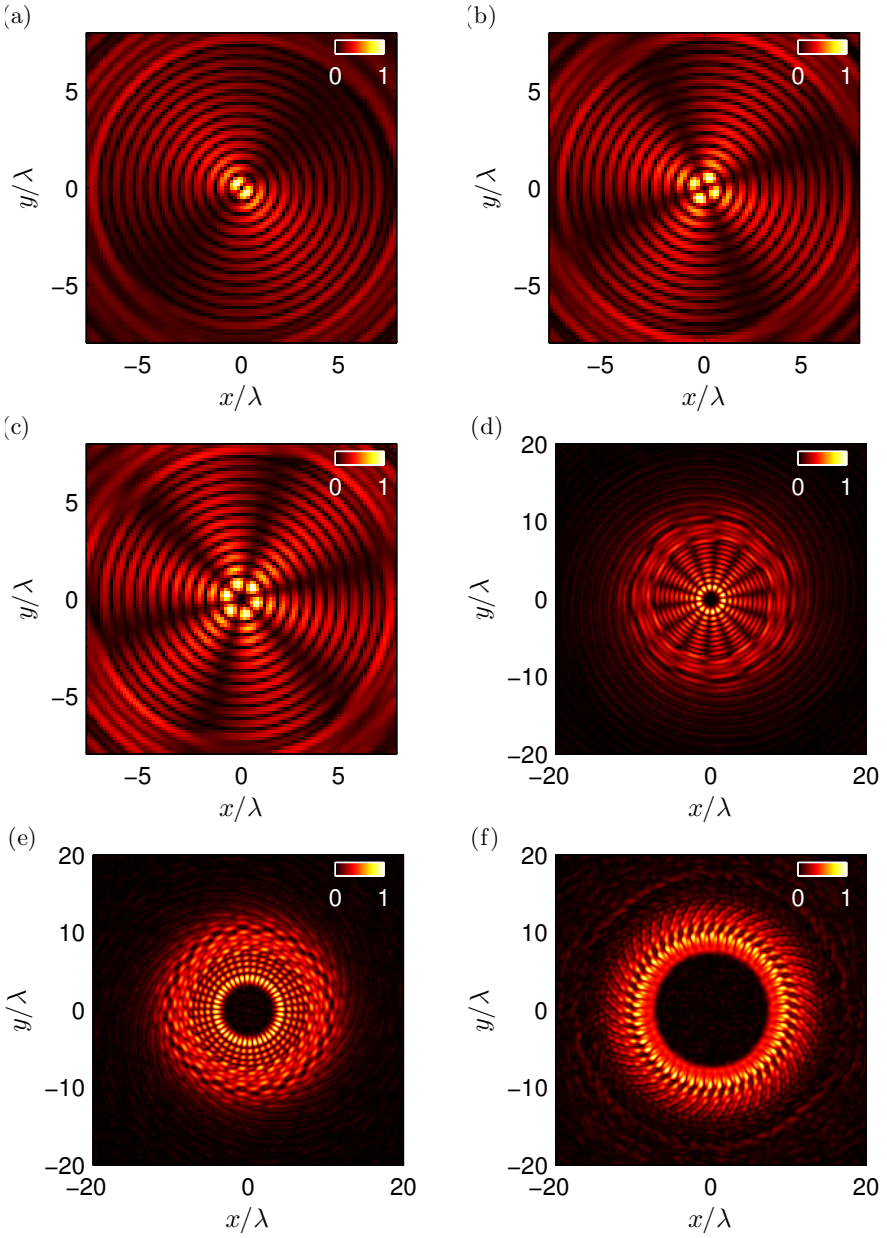


Figure 6.19: Magnitude of the field for the n-arm spiral grating, from (a-f), $n = 1, 2, 3, 7, 20, 50$ obtained by k-space numerical simulation. Colorbars in $p/p_{\max}$ units.

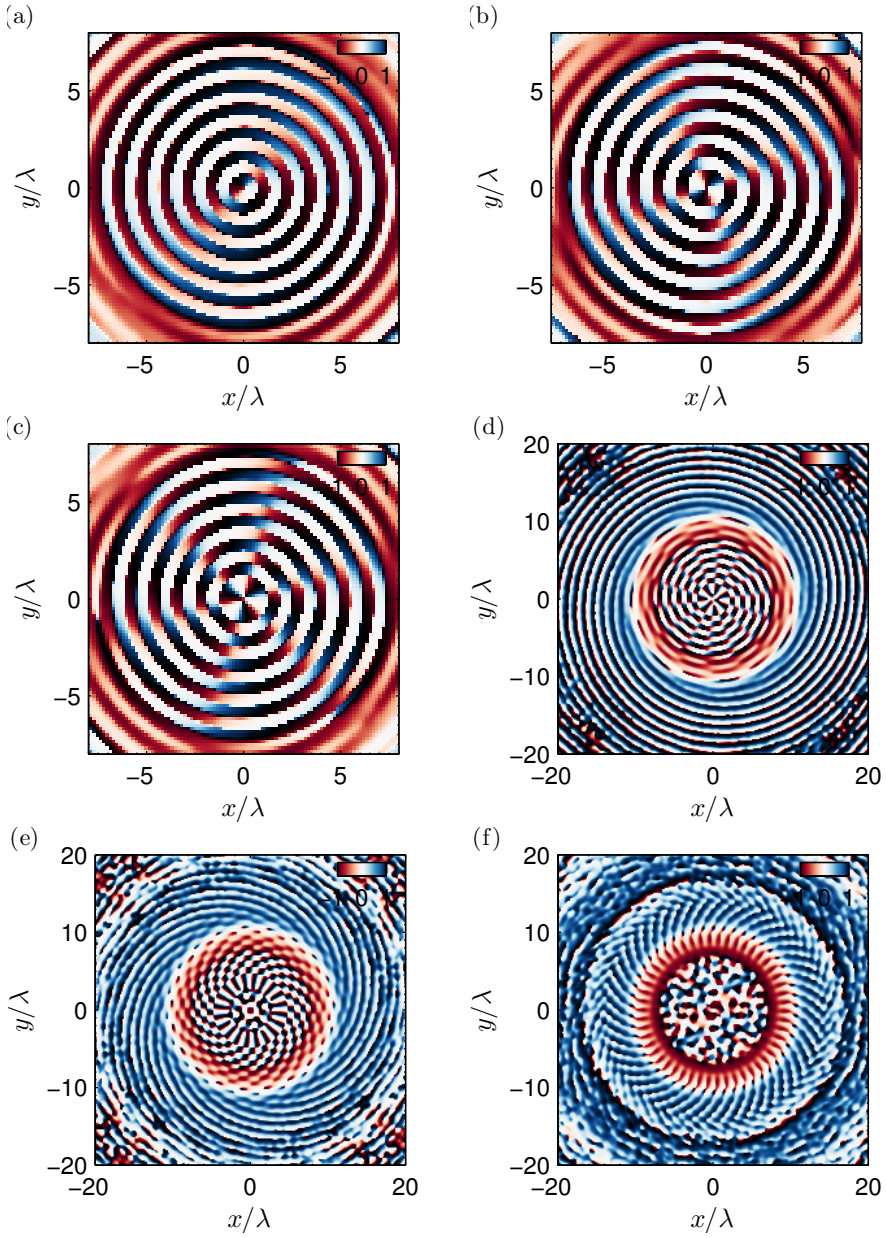


Figure 6.20: Phase of the field for the n-arm spiral grating, from (a-f), $n = 1, 2, 3, 7, 20, 50$ obtained by k-space numerical simulation. Colorbars in ϕ/π units.

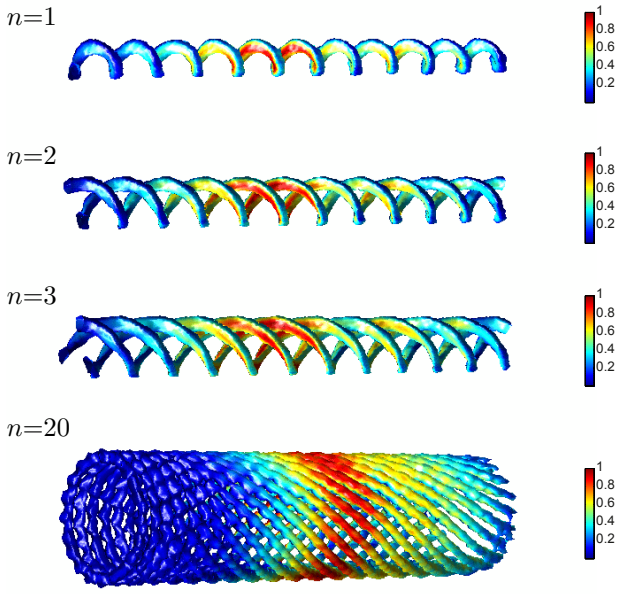


Figure 6.21: Reconstruction of the helical vortex by an isosurface of field points with equal phase. The number of helix arms is equal to the number of spiral arms of the gratings. Colorbars in $p/p_{\max}$ units.

simulations, instead of considering the scatterers perfectly rigid, the grating was included as a stainless steel plate, with same parameters than in the previous experimental setup. Thus, longitudinal wave propagation over the bulk of the steel plane were included. However, shear waves were not included in the simulations for the sake of simplicity. The simulation parameters used for the water media were $c_0 = 1490$ m/s and $\rho_0 = 1000$ kg/m^3 and for the grating plate $c_0 = 6100$ m/s and $\rho_0 = 7850$ kg/m^3. Losses were neglected in both media. Figure 6.18 shows the analytical HOBBs and the simulations of the proposed steel spiral gratings. Excellent agreement is obtained between the theory and the realistic simulations. Due the finite size of the structure, in this cases reduced to $R_{\max} = 25a$, the truncation effect of the Bessel function is more evident, as can be observed in the mismatching of the farther lateral lobes of the simulated beam. Furthermore, the characteristic oscillations of the maxima due to the helix focusing are more evident, as can be observed clearly in Fig. 6.19. It is worth noting here that those maxima are static, at this transversal cut ($z = F/2$), but rotates when the measurement is realized in a different plane according a multiple branch helix.

Concerning the vortex phase, the field also rotates with a topological charge equal to the spiral number of arms. Only in the case of $n = 50$ the beam is roughly generate. This effect is related to the finite sized aperture grating, where the cone

barely cover the volume necessary to generates the 18λ diameter of the ring shaped beam. However, even in this situation the central dark spot is generated, due to at the axis the conical wavefront always covers the volume for $z < F$. Those results evidence the feasibility of high order Bessel beam generation by spiral grating in realistic configurations.

6.5 Weakly nonlinear chiral beams

The nonlinear propagation of acoustic vortex have been studied previously. Most of these studies employs arrays of transducers to electronically modify the phase profile at the source plane. Acoustic vortex beams including shocks has been tested numerically and experimentally, where rotational shock waves have been generated. If nonlinear effects are produced in the propagation path and not near or inside the spiral grating, the propagation of electronically generated beams and the diffraction grating HOBBs proposed here will present high similarities.

We present simulations of the full-wave Eqs (3.1, 3.2, 3.3). The grating is designed as in previous simulations, where the nonlinearity of the water is introduced by the nonlinear parameter $B/A = 5$. Nonlinearity in the bulk of the steel plate is neglected. As Figs (6.22-6.22) shows, nonlinear acoustic vortex are produced in a similar fashion than in the preceding sections. However, in order to correctly account for higher spectral components, the numerical grid have been refined compared to the numerical results presented below. Due to the computation requirements of the resulting 3D problem, the total size of the domain of integration has to be reduced, and therefore, the total aperture, i.e. the number of turns of the spiral, has been reduced dramatically. In this section, the grating spiral is composed by only by 5 turns. These computational limitation impedes the calculation of higher Bessel beams due to the ring lateral lobes falls out of the domain. Other restriction of the full 3D nonlinear numerical problem is that the number of harmonics is very limited, and therefore, the simulations only can take into account weakly nonlinear propagation.

However, the basic features of the nonlinear vortex up to $n = 5$ can be presented. Figure 6.22 shows the magnitude of the first and its second harmonic transversal field distribution. It can be observed that due to the limited aperture grating, the Bessel beam is not correctly formed, but it can be appreciated how the characteristic lateral lobes appears. The zero at the axis roughly appears for the first and third order Bessel-like beams. In the case of $n = 5$ cannot be formed correctly. Here, the focalization of each spiral arm that creates n modulations over the lateral maxima is more evident. Again, if the measurement plane is shifted a small increment in z axial direction, those maxima rotates. Thus, the maxima conforms an n-helix curve. The second harmonic field generated in propagation also focuses on these maxima. In addition, second harmonic field also present additional modulations in the positions between the first harmonic modulations,

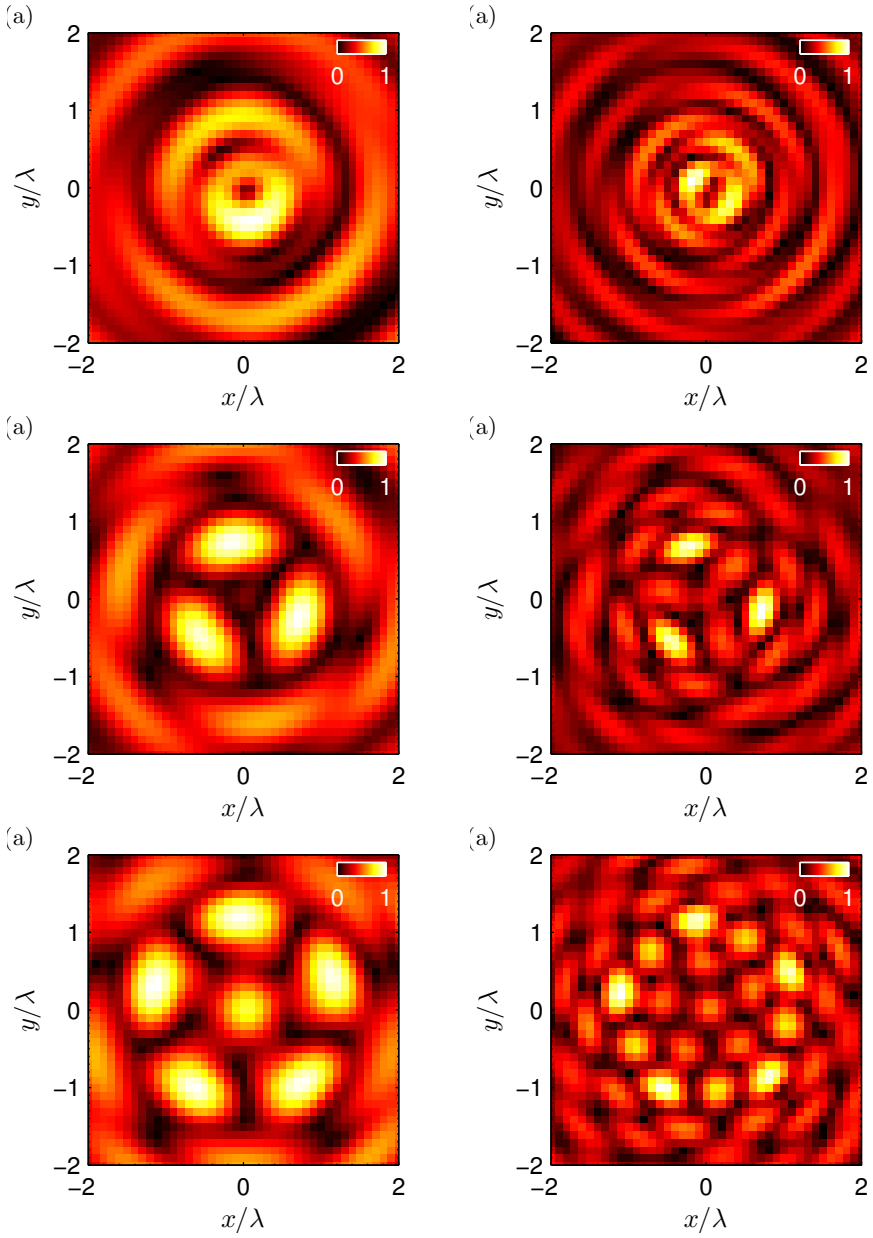


Figure 6.22: Magnitude of the field for the n-arm spiral grating, from top to bottom $n = 1, 3, 5$, (left column) first harmonic, (right column) second harmonic. Colorbars in $p/p_{\max}$ units.

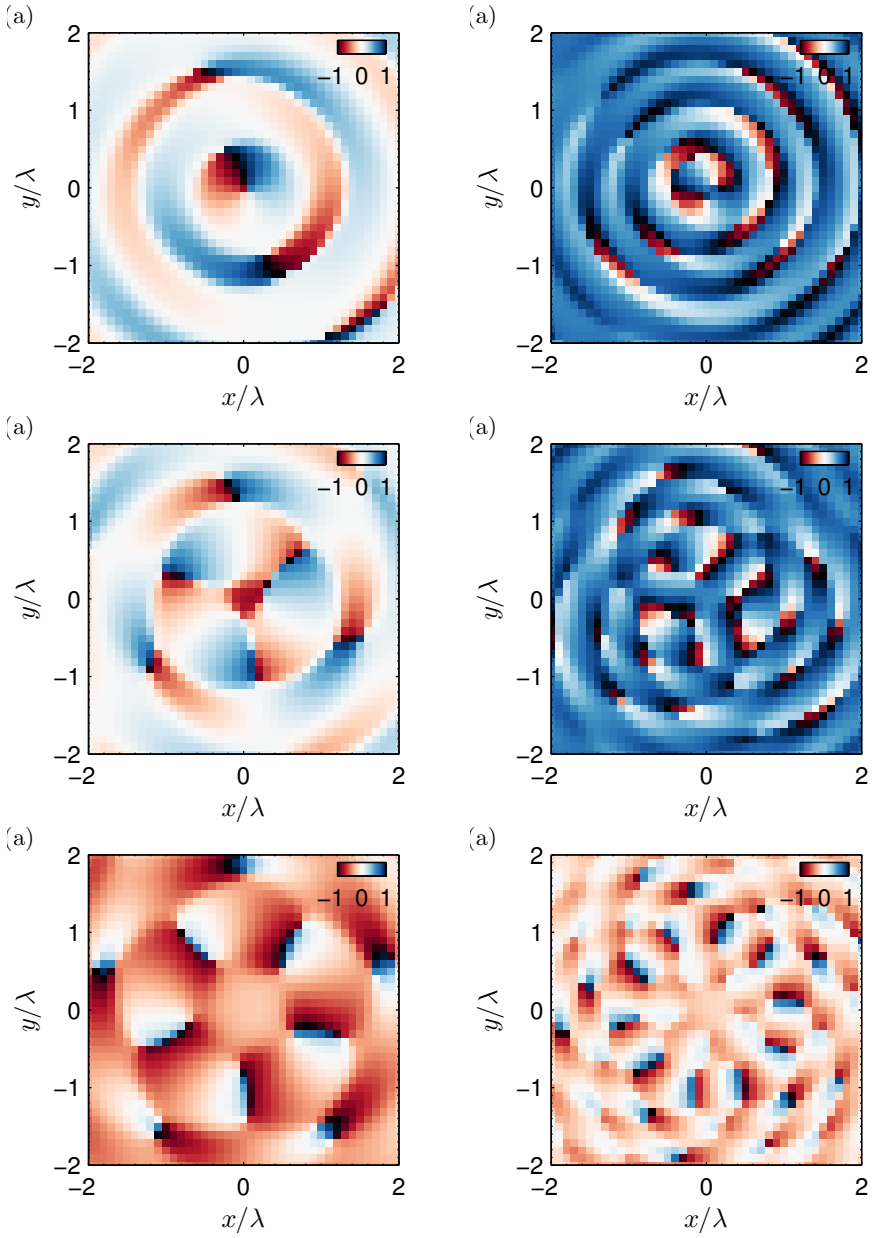


Figure 6.23: Phase of the field for the n-arm spiral grating, from top to bottom $n = 1, 3, 5$, (left column) first harmonic, (right column) second harmonic. Colorbars in ϕ/π units.

being these last of lower amplitude. Therefore, focalization around the axis of the higher harmonics are also helix shaped: the number of helix curves is the product of the harmonic index and the Bessel order.

Although the magnitude distribution of the field by this truncated grating hardly agrees to an ideal Bessel beam, the rotation of phase distribution is in agreement with the analytical vorticity of HOBBs. Thus, is clearly visible that the first harmonic in the simulations present a topological charge of n for the presented cases. In the case of second harmonic it rotates with topological charge $2n$. The topological charge is therefore the product of the the harmonic number and the order of the Bessel, i.e. the product of the harmonic and the number of arms. Thus, the conservation law for the ratio between the topological charge of the beam and the generated harmonic order is also observed (Marchiano et al., 2008). In this sense, nonlinearity present a opportunity to increase the topological charge of a generated beams.

Intensity vortex

One remarkable feature of the generated vortex is the acoustic intensity field. Due to the vortex rotation, the acoustic intensity vector presents, in addition to the axial, a rotational azimuthal component. The existence of this component evidences the possibility of using the HOBBs to transfer angular momentum to the media. Figure 6.24 presents an example of the transversal intensity distribution. The magnitude of the intensity maintains the characteristic ringed shape of the Bessel beam profile, wile the pointing vector of the intensity rotates around the axis.

The transfer of momentum from a wave to the media is closely related to the acoustic radiation force field. In the case of acoustic radiation force generated by scattering processes, i.e. when the gradient of the acoustic energy density is not null due to reflection on surfaces or objects, Bessel beams have been demonstrated high potential to generate interesting configurations for particle manipulation where negative axial radiation forces have been observed. On the other hand, if the gradient of the acoustic energy density is not null due to attenuation processes, there appears also a radiation force field. For plane waves, the acoustic radiation force exerted in the bulk of the lossy media is directly proportional to the intensity vector. The generated beams with acoustic intensity vortex can offer great potential in practical applications that uses acoustic radiation force generated by both, scattering or attenuation processes. The nonlinear acoustic radiation force will be studied in detail in Chapter 9 in the case of lossy media with frequency power law attenuation.

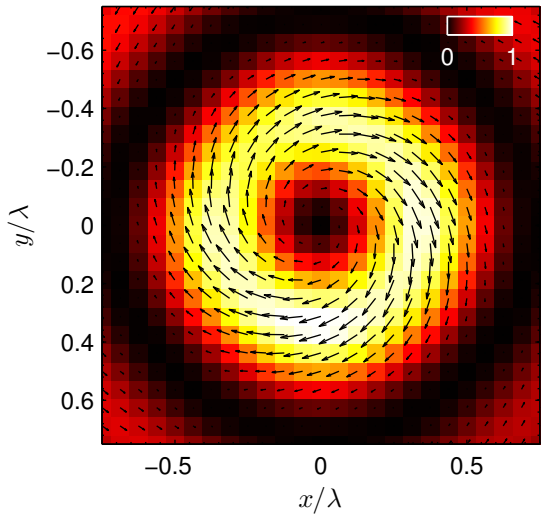


Figure 6.24: Intensity of a first order Bessel-like beam generated by a grating spiral. Colormap in $I/I_{\max}$ units, (arrows) intensity pointing vectors.

6.6 Conclusions

We have studied the scattering of Archimedes' spiral gratings, and demonstrated theoretically, experimentally and by numerical simulations that these diffraction gratings generates chiral beams. These beams are basically truncated high order Bessel beams, and are characterized by a null in the field all over it axis. It is demonstrated how the geometrical focal surrounds the axis in an helix shaped curve. It is of special interest the method presented for generation of arbitrary nth-order Bessel beams using regular spiral patters with n-arms or arms. It was shown that the order of the Bessel beam is directly the number of arms of the spiral. The radial position of the ringed lateral lobes grows with the order of the Bessel beam, and over it an acoustic vortex is generated. The topological charge of these vortex was also proportional to the number of arms of the spiral. Furthermore, we have demonstrated that another way to generate HOBBs is using higher diffraction orders, but this approach generates also secondary secondary beams along the axis and the energy spreads into all. Finally, The topological charge can be also increased by cumulative nonlinear effects, where the number of the harmonic is proportional to the product between the number of arms and the harmonic index.

The spiral diffraction gratings offers the possibility of dramatically increase the order of the beam by using together the mentioned effects. Thus, a grating made of high number of gratings can radiated with high frequency wave in order to excite superior diffraction orders. Finally, the ith-harmonic will present a topological

charge of inN, increasing its rotation and the possibility of transferring angular momentum to the media. On the other hand, currently work is being developed applying the technique of period varying grating exposed in Chapter 5 to an spiral configuration in order to achieve focusing of the vortex.

The presented method for synthesize HOBBs presents a high potential in ultrasound particle manipulation techniques and, in general, in acoustic radiation force applications in which the HOBBs have attracted great interest. This method provides the possibility of generation arbitrary order Bessel beams by a passive and extremely cheap device compared to active multiarrays. The generation of acoustic vortex by active means is limited by the amount of elements and its size. In contrast, the beam resolution by the proposed gratings is limited by the size of the scatterers and the space between them. Nowadays, with the increase in the performance of 3D printing and laser cutting techniques, the generation if HOBBs offer far more possibilities than its active counterpart to generate acoustical vortex.

References

Arlt, J and K Dholakia (2000). "Generation of high-order Bessel beams by use of an axicon". In: *Optics Communications* 177.1, pp. 297–301.

Bekshaev, A Ya and AI Karamoch (2008). "Displacements and deformations of a vortex light beam produced by the diffraction grating with embedded phase singularity". In: *Optics Communications* 281.14, pp. 3597–3610.

Brunet, Thomas, Jean-Louis Thomas, Régis Marchiano, and François Coulouvrat (2009). "Experimental observation of azimuthal shock waves on nonlinear acoustical vortices". In: *New Journal of Physics* 11.1, p. 013002.

Brunet, Thomas, Jean-Louis Thomas, Régis Marchiano, and François Coulouvrat (2010). "Experimental investigation of 3D shock waves on nonlinear acoustical vortices". In: *Physics Procedia* 3.1, pp. 905–911.

Demore, Christine, Zhengyi Yang, Alex Volovick, Han Wang, Sandy Cochran, Mike MacDonald, and Gabriel Spalding (2011). "A sonic screwdriver: Acoustic angular momentum transfer for ultrasonic manipulation". In: *Ultrasonics Symposium (IUS), 2011 IEEE International*. IEEE, pp. 180–183.

Durnin, Já, JJ Miceli Jr, and JH Eberly (1987). "Diffraction-free beams". In: *Physical Review Letters* 58.15, p. 1499.

Gspan, Stefan, Alex Meyer, Stefan Bernet, and Monika Ritsch-Marte (2004). "Optoacoustic generation of a helicoidal ultrasonic beam". In: *The Journal of the Acoustical Society of America* 115.3, pp. 1142–1146.

Heckenberg, NR, R McDuff, CP Smith, and AG White (1992). "Generation of optical phase singularities by computer-generated holograms". In: *Opt. Lett* 17.3, pp. 221–223.

Hefner, Brian T and Philip L Marston (1999). "An acoustical helicoidal wave transducer with applications for the alignment of ultrasonic and underwater systems". In: *The Journal of the Acoustical Society of America* 106.6, pp. 3313–3316.

Jimenez, Noe, Vicente Romero-García, R Picó, A Cebrecos, Víctor José Sánchez-Morcillo, LM Garcia-Raffi, Juan Vicente Sánchez-Pérez, and K Staliunas (2014). "Acoustic Bessel-like beam formation by an axisymmetric grating". In: *EPL (Europhysics Letters)* 106.2, p. 24005.

Marchiano, Régis, François Coulouvrat, Lili Ganjehi, and Jean-Louis Thomas (2008). "Numerical investigation of the properties of nonlinear acoustical vortices through weakly heterogeneous media". In: *Physical Review E* 77.1, p. 016605.

Marston, Philip L (2006). "Axial radiation force of a Bessel beam on a sphere and direction reversal of the force". In: *The Journal of the Acoustical Society of America* 120.6, pp. 3518–3524.

Marston, Philip L (2007a). "Negative axial radiation forces on solid spheres and shells in a Bessel beam". In: *The Journal of the Acoustical Society of America* 122.6, pp. 3162–3165.

Mitri, FG (2008). "Acoustic scattering of a high-order Bessel beam by an elastic sphere". In: *Annals of Physics* 323.11, pp. 2840–2850.

Mitri, FG (2009). "Negative axial radiation force on a fluid and elastic spheres illuminated by a high-order Bessel beam of progressive waves". In: *Journal of Physics A: Mathematical and Theoretical* 42.24, p. 245202.

Mitri, FG, TP Lobo, and GT Silva (2012). "Axial acoustic radiation torque of a Bessel vortex beam on spherical shells". In: *Physical Review E* 85.2, p. 026602.

Molerón, M., A. Leonard, and C. Daraio (2014). "Solitary waves in a chain of repelling magnets". In: *J. Appl. Phys.* 115.18, p. 184901.

Nye, JF and MV Berry (1974). "Dislocations in wave trains". In: *Proceedings of the Royal Society of London A: Mathematical, Physical and Engineering Sciences*. Vol. 336. 1605. The Royal Society, pp. 165–190.

Oemrawsingh, S. S. R., J. A. W. van Houwelingen, E. R. Eliel, J. P. Woerdman, E. J. K. Verstegen, J. G. Kloosterboer, and G. W. 't Hooft (2004). "Production and characterization of spiral phase plates for optical wavelengths". In: *Appl. Opt.* 43.3, pp. 688–694.

Romero-García, Vicente, R Picó, A Cebrecos, Víctor José Sánchez-Morcillo, and K Staliunas (2013). "Enhancement of sound in chirped sonic crystals". In: *Applied Physics Letters* 102.9, p. 091906.

Schwarz, Thomas (2013). "Rotation of particles by ultrasonic manipulation". PhD thesis. Diss., Eidgenössische Technische Hochschule ETH Zürich, Nr. 21572, 2013.

Skeldon, KD, C Wilson, M Edgar, and MJ Padgett (2008). "An acoustic spanner and its associated rotational Doppler shift". In: *New Journal of Physics* 10.1, p. 013018.

Thomas, Jean-Louis and Régis Marchiano (2003). "Pseudo angular momentum and topological charge conservation for nonlinear acoustical vortices". In: *Physical review letters* 91.24, p. 244302.

Vasara, Antti, Jari Turunen, and Ari T Friberg (1989). "Realization of general nondiffracting beams with computer-generated holograms". In: *JOSA A* 6.11, pp. 1748–1754.

Wu, Junru (1991). "Acoustical tweezers". In: *The Journal of the Acoustical Society of America* 89.5, pp. 2140–2143.

Yoon, Changhan, Bong Jin Kang, Changyang Lee, Hyung Ham Kim, and K Kirk Shung (2014). "Multi-particle trapping and manipulation by a high-frequency array transducer". In: *Applied physics letters* 105.21, p. 214103.

Publications

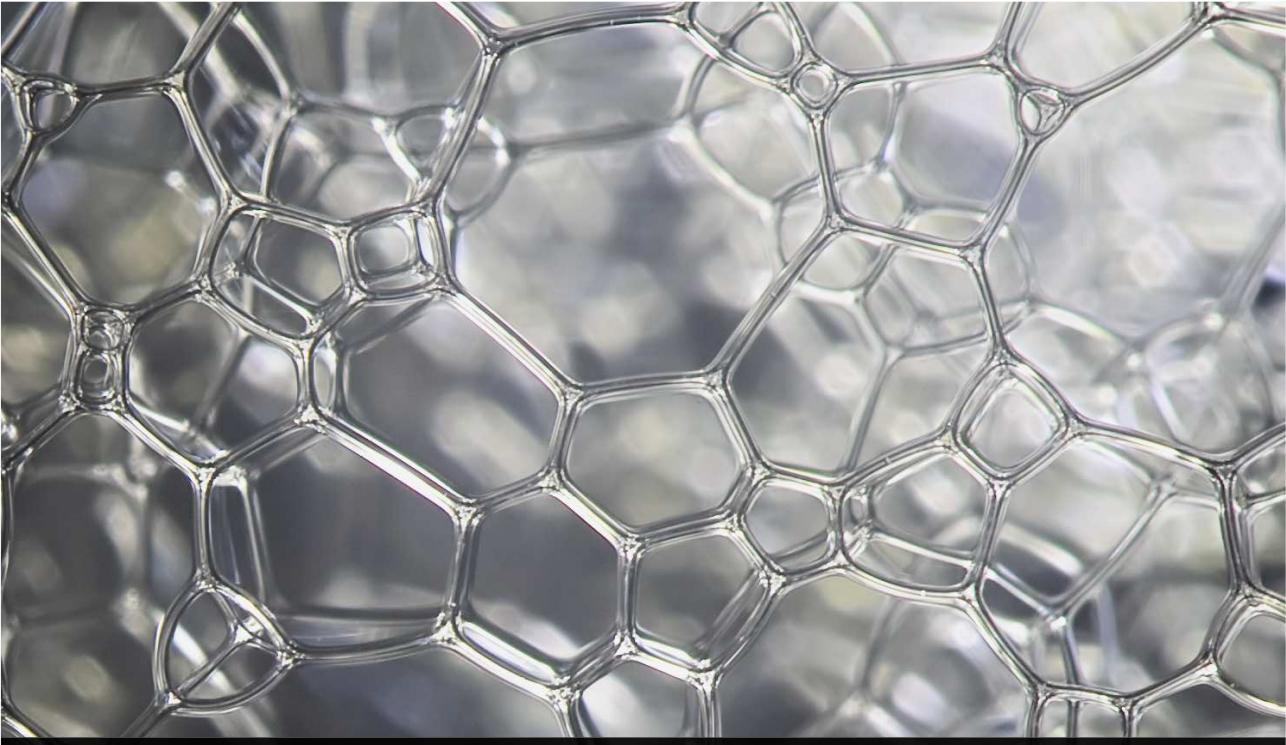
The contents of this chapter have been presented in the following publications:

Journal papers

- **N. Jimenez**, V. J. Sanchez-Morcillo, R. Pico, L. Garcia-Raffi, V. Romero-Garcia and K. Staliunas "High-order acoustic Bessel beam generation by spiral gratings" *Ultrasonics*, *In preparation*

Conference proceedings

- **N. Jimenez**, V. J. Sanchez-Morcillo, R. Pico, L. Garcia-Raffi, V. Romero-Garcia and K. Staliunas "High-order acoustic Bessel beam generation by spiral gratings" *2015 International Congress on Ultrasonics*, Metz, France. May 10-15, (2015)



Part II

Nonlinear Acoustic Waves in Biological Media

